Macromolecules

Article

pubs.acs.org/Macromolecules

Solvent-Regulated Mesoscale Aggregation Properties of Dilute PBTTT-C_{14} Solutions

Han L. Yi, Ching H. Wu, Chun I Wang, and Chi C. Hua*

Department of Chemical Engineering, National Chung Cheng University, Chiayi 62102, Taiwan, ROC

Supporting Information

ABSTRACT: Contrasting mesoscale aggregate features of a promising conjugated polymer, poly(2,5-bis(3-tetradecylthiophene-2-yl)thieno[3,2-*b*]thiophenes) (pBTTT-C_{14}), that result from the use of two slightly different aromatic solvents, i.e., toluene and chlorobenzene, for a range of dilute solutions (0.5−1.2 mg/mL) are systematically explored using depolarized dynamic light scattering (DDLS), dynamic/static light scattering (DLS/SLS), small-angle X-ray scattering (SAXS), and scanning transmission electron/scanning electron/transmission electron microscopy (STEM/SEM/TEM) analysis schemes. The central findings are as follows: (1) DDLS and all EM features reveal that whereas pBTTT-C_{14} aggregate clusters fostered in toluene (a poorer solvent) are moderately anisotropic (cylindrical; aspect ratio ∼3) in shape, they are nearly isotropic (spherical) in chlorobenzene (a better solvent), with mean sizes in the range of a few hundred nanometers. (2) Combined DDLS/DLS/SLS/SAXS analyses indicate that the aggregate clusters in both solvent media are coexistent with a certain fraction of small rod-like species (∼10 nm in length; aspect ratio ∼2), similar or even identical to the packing units which build up the fractal network of an aggregate cluster. (3) Accurate atomistic molecular dynamics (AMD) simulations of one- and five-chain aggregate systems reveal that the solvent-induced, contrasting nanoscale/mesoscale aggregate features bear a *dynamic* origin, through the backbone torsional relaxation that substantially impacts the bolstering interaction force (van der Waals vs $\pi-\pi$) and, hence, the "anisotropic persistence" of the fundamental packing units. (4) The overall features suggest that different organic solvents may be utilized to engineer the (mesoscale) size and shape as well as the (nanoscale) packing units of the aggregate species incubated in solution and shed light on the morphological developments during thin-film fabrication that have been the focus of recent research on the pBTTT-C_n series.

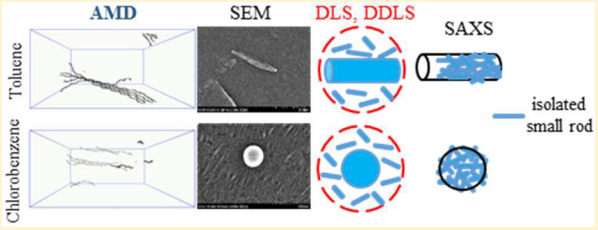

1. INTRODUCTION

Poly(2,5-bis(3-alkylthiophen-2-yl)thieno[3,2-*b*]thiophenes) (pBTTTs) represent a promising class of conjugated polymers due to their high charge carrier mobility[1−5] and good oxidative stability[1] for applications in organic photovoltaic cells (OPVs)[6,7] and organic thin-film transistor (OTFT).[8] Recently, there has been a fast-growing number of experimental and theoretical investigations into the molecule-scale packing of pBTTT-C_n using a variety of characterization schemes, including near-edge X-ray absorption fine structure (NEXAFS) and infrared (IR) absorption spectroscopies,[4] X-ray diffraction (XRD),[2,5,9] grazing incidence X-ray diffraction (GIXD),[10] density functional theory (DFT) calculations,[11] and molecular mechanics (MM) simulations.[12,13] Still others demonstrated that the thin-film microstructure of pBTTT-C_n can have a significant impact on their electronic properties, by varying the molecular weight of pBTTT,[14−17] their side-chain length,[9,13] and the casting solvent,[18−22] or simply through post-treatments of thermal annealing.[2,10,22−24] These studies, as a whole, contributed to the revelation of five representative types of morphological development: fiber (or rod-like) formation,[14,16,18,19] nodule (or particle-like) feature,[2,24] terrace (or disc-like) formation,[2,11,15,16,21,24] ribbon phase,[10,23,25] and rough morphology,[16] mainly through atomic force microscopy (AFM) characterizations.

To date, however, relatively few investigations have been dedicated to exploring the role of solution-state properties during thin-film formation. Zhao et al.[15] explored the role of pBTTT-C_{14} molecular weight during the formation of "unentangled π-stacking" in the chlorobenzene medium, as a precursor for the subsequent development of monolayer-terraced morphology in thin film; they suggested that pBTTT-C_{14} chains in dilute chlorobenzene (1−4 mg/mL) first adopt random-coil conformation necessary for an effective chain packing at a later stage. Wang et al.[20] reported results on Franck−Condon analysis of the absorption spectra, revealing the formation of distinct aggregation states with the use of different solvent media (i.e., *o*-dichlorobenzene (*o*-DCB), chlorobenzene, toluene, and mixed xylenes). Wang et al.[18,19] investigated the formation of nanofibrils for a series of P3ATs derivatives including pBTTT, through solvent-vapor annealing and by adding different additives in solution. They reported on coexistent pBTTT-C_{12} chains and aggregates in dilute *o*-DCB

Received: April 16, 2017
Revised: June 4, 2017
Published: July 11, 2017

ACS Publications © 2017 American Chemical Society

DOI: 10.1021/acs.macromol.7b00790
Macromolecules 2017, 50, 5498−5509

solution (0.1 mg/mL) from dynamic light scattering analysis. Recently, Gaikwad et al.[21] scrutinized the effect of solvent media on the surface roughness of solution-processed thin films. Similar, although sporadic, efforts have been devoted to several other conjugated polymers including PFs series,[26,27] PPV series,[28,29] and P3HT series,[30−33] for a general understanding of the relationships between solution-state microstructure and thin-film morphology.

Given that the thin-film morphology of pBTTT-C_n has been shown to depend critically on the processing techniques and, in particular, the solvent media used, it seems imperative to disclose the pathway in which different solvent media impact the nanoscale/mesoscale aggregate features that through the subsequent processing would ultimately determine the charge transport properties of a thin-film device. Herein, we conduct the first in-depth investigation into the multiscale aggregate features of pBTTT-C_{14} using a comprehensive combination of analysis schemes, including depolarized dynamic light scattering (DDLS), dynamic light scattering (DLS), and static light scattering/small-angle X-ray scattering (SLS/SAXS), along with various electron microscopy (EM) images. While DDLS, DLS, SLS, and SAXS analyses are capable of providing detailed aggregate features in solution over a broad range of length and time scales, EM characterizations help further correlate the solution properties with the thin-film morphology. Intriguingly, we report on the central finding that the use of two slightly different aromatic solvents, chlorobenzene (CB) and toluene (T), leads to distinct mesoscale aggregation features in pBTTT-C_{14} solution and thin film. Accurate atomistic molecular dynamics (AMD) simulations further reveal that the two solvent media impact the single-chain and aggregate properties of pBTTT-C_{14} through a *dynamic* backbone relaxation process—contrary to the often assumed static interactions as might be explained, for instance, by the notion of Hansen solubility parameters. The overall findings clearly suggest that different types of organic solvents can be used to engineer the (mesoscale) size and shape as well as the (nanoscale) packing units of the aggregate species in solution and thin film. The knowledge should help bridge the gap between solution-state features and the previously reported, somewhat enigmatic, morphological developments of pBTTT-C_n during thin-film formation.

2. EXPERIMENTAL METHODS

2.1. Materials and Sample Preparation. The poly[2,5-bis(3-tetradecylthiophen-2-yl)thieno[3,2-*b*]thiophene] (pBTTT-C_{14}) sample (M_w = 59 771 g/mol, PDI = 4.15; see the chemical structure in Figure 1) was purchased from Luminescence Technology Corp. (Taiwan) and used without further purification. The solvent for dissolving pBTTT-C_{14}, chlorobenzene (CB; Sigma-Aldrich, USA, ≥99.5% in purity), or toluene (T; Merck, Germany, ≥99.0% in purity) was filtered through a 0.22 μm PVDF filter (Millipore Millex-GN) to remove dust. The sample vials used in all experiments were washed with detergent and then treated with filtered deionized water. To expedite the dissolution process, dilute pBTTT-C_{14} solutions (0.5, 0.9, and 1.2 mg/mL) in CB or T were sonicated for 12 h at 70.0 °C,[28,34] whereby transparent and homogeneous solutions were obtained. The two solvent media were utilized because CB is among the best solvents for spin-coating due to its high boiling point, while T represents a commonly used aromatic solvent for dissolving conjugated polymers. The resulting solution was further filtered into dust-free vial using 0.45 μm PVDF filter and was allowed to equilibrate for at least 1 h at room temperature before being transferred to the sample carriers for subsequent characterizations.

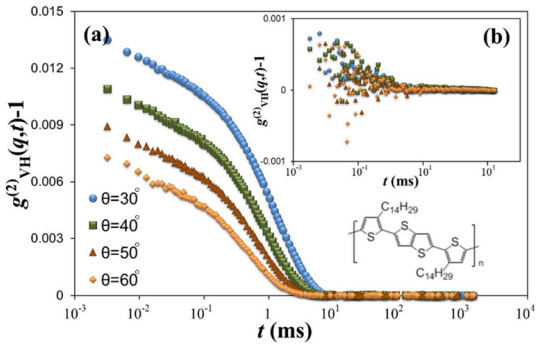

Figure 1. Depolarized intensity autocorrelation functions, $g^{(2)}_{VH}(q,t) - 1$, for pBTTT-C_{14} in (a) toluene and (b) chlorobenzene (inset) media at 0.9 mg/mL and T = 25.0 °C, where different symbols represent the results from four different scattering angles. The chemical structure of pBTTT-C_{14} is inserted in the figure.

2.2. Light Scattering (DLS/SLS) Analyses. Light scattering (LS) measurements were performed on a laboratory-built apparatus as described elsewhere;[35,36] a 34 mW polarized He−Ne laser (λ_0 = 632.8 nm; Lasos, LGK 7626 S) was used as the incident light, at which pBTTT-C_{14} solutions show negligible absorption (see Supporting Information Figure S1). The vial containing the sample solution of 2 mL in volume is a cylindrical quartz cell with 1 cm in diameter (Hellma, 540.111, Germany); a cap is utilized to prevent solvent evaporation during the entire experiment. All measurements were conducted at 25.0 ± 0.1 °C for a range of scattering angles θ = 30°−140°.

In the SLS experiment, the angular dependence of the excess time-averaged (for a duration of scanning of 15 s) scattering intensity, described by the relation $I_{ex}(q) = [I_{solu}(q) - I_{solv}(q)]/I_{tol}(q)]$, was investigated, where I_{solu} and I_{solv} denote the time-averaged scattering intensities of the solution and solvent, respectively, and I_{tol} is the average scattering intensity of toluene measured in the same apparatus; $q = (4\pi n_0/\lambda_0)\sin(\theta/2)$ is the scattering wave vector with λ_0 (=632.8 nm) being the wavelength of the incident beam and n_0 the refractive index of the solvent.

In the DLS experiment, the normalized intensity autocorrelation function, $g^{(2)}(q,t)$, was collected in a homodyne mode, which is related to the normalized field autocorrelation function, $|g^{(1)}(q,t)|$, through the Siegert relation[37]

$$g^{(2)}(q, t) = 1 + \beta |g^{(1)}(q, t)|^2 \quad (1)$$

where t is the decay time of the autocorrelation function, and β ($0 < \beta < 1$) is the spatial coherence factor. For multiple-mode relaxation processes, the field autocorrelation function, $|g^{(1)}(q,t)|$, can be related to the decay rate distribution, $G(\Gamma)$, by the Laplace transformation:

$$|g^{(1)}(q, t)| = \int_0^\infty G(\Gamma)\exp(-\Gamma t)\, d\Gamma \quad (2)$$

where the detailed distribution $G(\Gamma)$ may be obtained by inverse Laplace transformation using the commercial software CONTIN.[38] For a diffusion process, $\langle\Gamma\rangle$ can be related to the mean translational diffusion coefficient, $\langle D_T\rangle$, by $\langle D_T\rangle = (\langle\Gamma\rangle/q^2)_{q\to 0}$, and then the associated mean hydrodynamic radius $\langle R_h\rangle$ can be obtained using the Stokes−Einstein equation, $\langle R_h\rangle = k_B T/6\pi\eta\langle D_T\rangle$, where k_B is the Boltzmann constant and η is the solvent viscosity measured at the absolute temperature T.

2.3. Depolarized Dynamic Light Scattering (DDLS) Analysis. To assess the peculiar relaxation feature associated with anisotropic objects, DDLS measurements utilize incident light that is vertically polarized while the scattering light is horizontally polarized before entering the analyzer (Thorlabs, LPVIS050-MP2), with an extinction coefficient less than 10^{-5}. Thus, for anisotropic objects measured in a DDLS experiment, the polarized (VV), $|g^{(1)}_{VV}(q,t)|$, and depolarized (VH), $|g^{(1)}_{VH}(q,t)|$, normalized field autocorrelation functions were

DOI: 10.1021/acs.macromol.7b00790
Macromolecules 2017, 50, 5498−5509

collected at different scattering angles. The decay rates $\langle\Gamma\rangle$ obtained from polarized ($\langle\Gamma_{VV}\rangle = \langle D_T\rangle q^2$) and depolarized ($\langle\Gamma_{VH}\rangle = \langle D_T\rangle q^2 + 6\langle D_R\rangle$) dynamic light scattering may be expressed by

$$|g^{(1)}{}_{VV}(q, t)| = \exp[-\langle\Gamma_{VV}\rangle t] + k \exp[-\langle\Gamma_{VH}\rangle t] \quad (3)$$

$$|g^{(1)}{}_{VH}(q, t)| = \exp[-\langle\Gamma_{VH}\rangle t] \quad (4)$$

where $\langle D_T\rangle$ and $\langle D_R\rangle$ above denote the mean translational and rotational diffusion coefficients, respectively, and k is a constant dependent on the characteristics of the optical anisotropy of the probed object (i.e., $qL > 3$; L denotes the length) and is zero for isotropic objects (i.e., $qL < 3$).[39]

2.4. Small-Angle X-ray Scattering (SAXS) Analysis. SAXS measurements were carried out at beamline BL23A1 station of the National Synchrotron Radiation Research Center (NSRRC) in Taiwan. The scattering X-ray covers a q-range of 0.04−3.2 nm^{-1}, with 15 keV incident beam (wavelength λ_0 = 0.827 Å) and sample-to-detector distance of 4352 mm. All measurements were conducted at 25 ± 0.1 °C.

2.5. Electron Microscopy (EM) Analyses. The pBTTT-C_{14} images were taken from a field emission scanning electron microscopy (FE-SEM; Hitachi S4800-I). The acceleration voltage was 15 kV, and the working distance was ∼8 mm. The samples were prepared by drop-casting onto a glass substrate and then dried at room temperature (for SEM imaging). To obtain more detailed information about the shape and dimension of pBTTT-C_{14} aggregates, the sample solution was filtered through a copper grid coated with carbon film, and the wetted grid was placed on a filter paper (ADVANTEC filter paper 1) to undergo natural drying at room temperature (for STEM and TEM imaging). The images of the resulting sample were taken in a transmission electron microscopy (JEOL JEM-2010) at an acceleration voltage of 200 kV.

3. RESULTS AND DISCUSSION

3.1. Mesoscale Features of pBTTT-C_{14} Aggregates. The DDLS analysis was first carried out to reveal the shapes of bulk pBTTT-C_{14} aggregates in two different solvent media: toluene and chlorobenzene. The depolarized intensity autocorrelation functions, $g^{(2)}{}_{VH}(q,t) - 1$, obtained for the two pBTTT-C_{14} solutions at a concentration of 0.9 mg/mL are presented in Figure 1. It can be seen that the $g^{(2)}{}_{VH}(q,t) - 1$ for pBTTT-C_{14}/toluene solution exhibits a clearly discernible relaxation pattern compared to that of pBTTT-C_{14}/chlorobenzene solution (shown in the inset), which produces no discernible signals within experimental uncertainty. Importantly, these features imply that whereas pBTTT-C_{14} aggregate clusters are notably anisotropic in shape in toluene, they are basically isotropic in chlorobenzene. Similar results can be noted at the other concentrations investigated (Figure S2). Detailed analyses of the underlying structural features are discussed below.

3.2. DLS/DDLS Features of pBTTT-C_{14} Aggregates in Toluene. The DDLS feature in Figure 1, and the EM images in Figure 10a discussed in a later section, indicate that the pBTTT-C_{14} aggregate clusters incubated in toluene assume a notably anisotropic shape. The corresponding field autocorrelation functions, $|g^{(1)}(q,t)|$, measured at different scattering angles are shown in Figures 2a and 3a for the VV and VH geometries, respectively. Similar features of the field autocorrelation function are observed at two other concentrations, as shown in Figures S3 and S4. The associated decay time distribution, $G(\tau)$ (= $G(1/\Gamma)$), clearly reveals the existence of two relaxation modes for both VV (Figure 2b) and VH (Figure 3b) geometries.

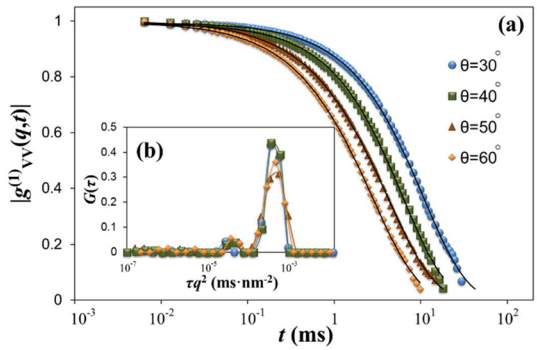

Figure 2. (a) Angular dependences of the field autocorrelation function, $|g^{(1)}{}_{VV}(q,t)|$, in the DLS experiment and (b) the relaxation time distributions, $G(\tau)$, retrieved from CONTIN as a function of τq^2 for the 0.9 mg/mL pBTTT-C_{14}/toluene solution. The fast mode corresponds to isolated small rods, and the slow mode represents cylindrical aggregate clusters. The full lines are nonlinear least-squares fits according to eq 5.

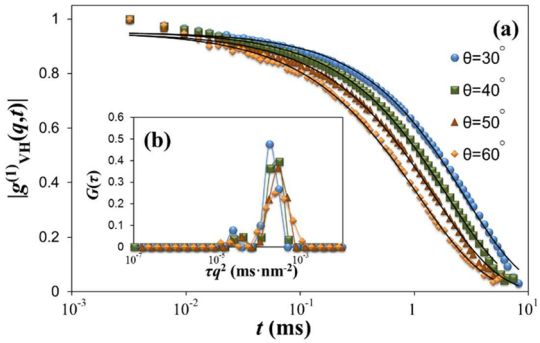

Figure 3. (a) Angular dependences of the field autocorrelation function, $|g^{(1)}{}_{VH}(q,t)|$, in the DDLS experiment and (b) the relaxation time distributions, $G(\tau)$, retrieved from CONTIN as a function of τq^2 for the 0.9 mg/mL pBTTT-C_{14}/toluene solution. The fast and slow modes have physical significances as in Figure 2. The full lines are nonlinear least-squares fits according to eq 6.

Previously, Wang et al.[18,19] reported on two relaxation modes for pBTTT-C_{12} in a variety of solvent media; they assigned the fast mode to the contribution of isolated chains and the slow mode to that of aggregates. According to eqs 3 and 4 and the expressions above, the mean decay rates, $\langle\Gamma\rangle$, for the fast and slow modes are plotted as a function of q^2 in Figure 4. Similar results can be noted at the other concentrations (Figure S5). We discuss first the significance of the fast mode. Figure 4a shows that there is a similar slope and a common intercept for the decay rates obtained from the VV and VH geometries, respectively. Recall that the slope reflects the translational diffusion coefficient, D_T, while the intercept is equal to 6 times the rotational diffusion coefficient, D_R. Clearly, the fast mode in the two experiments (DLS and DDLS) represents the same (rodlike) species. Next, we examine the features of the slow mode.

Figure 4b indicates that the VV decay rate, $\langle\Gamma_{VV,slow}\rangle$, is purely diffusive in nature, as the extrapolation to q = 0 passes through the origin. The slope again yields the translational diffusion coefficient, D_T. In contrast, the VH decay rate, $\langle\Gamma_{VH,slow}\rangle$, exhibits a relationship of the type $\langle\Gamma_{VH,slow}\rangle = D_T q^2 + 6D_R$. Although the two geometries yield approximately the same slope and thus D_T, confirming that the same (aggregate) species was being probed in both experiments, it is unclear why

DOI: 10.1021/acs.macromol.7b00790
Macromolecules 2017, 50, 5498−5509

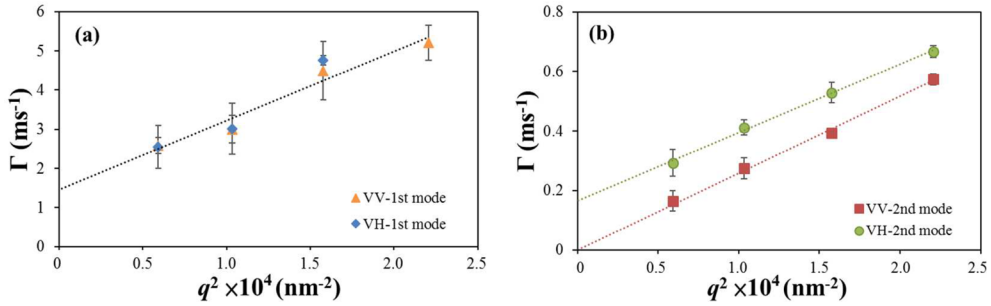

Figure 4. Mean decay rates, $\langle\Gamma\rangle$, as a function of q^2 for (a) the fast mode and (b) the slow mode for the 0.9 mg/mL pBTTT-C_{14}/toluene solution. The dotted lines represent the results of a linear regression.

Table 1. Parameter Values Extracted from a Global Fitting of DLS and DDLS Data on Several pBTTT-C_{14}/Toluene Solutions

			concentration (mg/mL)		
method			0.5	0.9	1.2
DLS	isolated small rod	length (L) [nm]	10.0 ± 1.1	11.3 ± 2.2	10.5 ± 0.9
		diameter (d) [nm]	4.5 ± 0.2	4.6 ± 0.2	5.1 ± 1.2
		stretch exponent (α)	0.99 ± 0.01	0.99 ± 0.01	0.98 ± 0.02
		aspect ratio	2.2	2.5	2.1
	cylindrical aggregate cluster	length (L) [nm]	320 ± 32	381 ± 50	435 ± 95
		diameter (d) [nm]	96 ± 17	124 ± 17	142 ± 22
		stretch exponent (β)	0.81 ± 0.03	0.83 ± 0.03	0.86 ± 0.05
		aspect ratio	3.3	3.1	3.1
	$W_{\text{isolated small rod}}$		0.90	0.85	0.80
DDLS	isolated small rod	length (L) [nm]	10.8 ± 1.4	10.0 ± 0.1	10.0 ± 0.2
		diameter (d) [nm]	4.8 ± 0.6	4.5 ± 0.1	4.6 ± 0.2
		stretch exponent (α)	0.72 ± 0.02	0.71 ± 0.01	0.71 ± 0.01
		aspect ratio	2.2	2.2	2.2
	cylindrical aggregate cluster	length (L) [nm]	559 ± 46	610 ± 36	614 ± 56
		diameter (d) [nm]	224 ± 14	230 ± 31	253 ± 34
		stretch exponent (β)	0.70 ± 0.01	0.79 ± 0.03	0.83 ± 0.07
		aspect ratio	2.5	2.7	2.4

the VV decay rate in the DLS experiment is unable to reveal the rotational movement as in Figure 4a for the fast mode. Our conjecture is that one requires, in general, that the inequality $6D_R \gg D_T q^2$ holds true for a manifest revelation of the rotational mode in the DLS (VV) experiment. This requirement is excellently fulfilled for the fast mode in Figure 4a, while one has $6D_R \sim D_T q^2$ for the slow mode in Figure 4b. A similar situation with the VV decay rate has been noted previously for multiwalled carbon nanotubes[40,41] and fractal aggregates.[42,43] In the following analysis, we show that the slow mode represents the contribution from cylindrical aggregate clusters, likely built up by small pBTTT-C_{14} rods that are similar or even identical to those underlying the fast mode.

In prior work using fluorescence correlation spectroscopy (FCS)[44] and dynamic/depolarized light scattering[45−47] analyses for gold nanorod suspensions, one typically observed two relaxation modes in the VV correlation functions. While the slow mode was attributed to the translation diffusion of the rods, the fast mode and the relaxation rates of the VH correlation functions were dominated by the rotational diffusion of the same rod species. In the present study, where two different rod species coexist, the corresponding relaxation modes in the DLS or DDLS experiment require a proper reformulation of the field autocorrelation function. Considering the central features in Figure 4, the following stretch-exponential functions are adopted to describe the DLS and DDLS data that account for a slight polydispersity in rod dimensions:

$$|g^{(1)}{}_{VV}(q, t)| = A \exp\{-[(D_{T,fast}q^2 + 6D_{R,fast})t]^{\alpha}\} + (1 - A) \exp\{-[(D_{T,slow}q^2)t]^{\beta}\} \quad (5)$$

$$|g^{(1)}{}_{VH}(q, t)| = A \exp\{-[(D_{T,fast}q^2 + 6D_{R,fast})t]^{\alpha}\} + (1 - A) \exp\{-[(D_{T,slow}q^2 + 6D_{R,slow})t]^{\beta}\} \quad (6)$$

Clearly, the first term in each equation describes the contributions of the fast mode and the second for the slow mode. The tactics for an unambiguous determination of the geometric features of pBTTT-C_{14} in solution by using this set of equations along with a full-curve fitting in Figures 2 and 3 (solid lines) are described in detail below.

First, the two diffusion coefficients (i.e., D_T and D_R) fitted in Figure 4 for the individual mode (fast or slow mode) can be used to determine the aspect ratio L/d of a rod or cylindrical object. A useful approximation for this purpose has been provided by Broersma[48] for the range of $\ln(L/d) > 2$. Because the previous requirement is not always fulfilled for the pBTTT-C_{14} solutions investigated, an alternative formulation proposed by Ortega and García de la Torre[49] for a wider range $2 < L/d < 20$ is adopted:

DOI: 10.1021/acs.macromol.7b00790
Macromolecules 2017, 50, 5498−5509

$$D_T = \frac{k_B T(\ln(L/d) + C)}{3\pi\eta L} \quad (7)$$

$$D_R = \frac{3k_B T(\ln(L/d) + C_r)}{\pi\eta L^3} \quad (8)$$

In these expressions, C and C_r denote second-order polynomials in L/d, the coefficients of which have been determined by fitting the numerical data to be

$$C = 0.312 + 0.565\frac{d}{L} - 0.10\left(\frac{d}{L}\right)^2 \quad (9)$$

$$C_r = 0.662 + 0.917\frac{d}{L} - 0.05\left(\frac{d}{L}\right)^2 \quad (10)$$

When eqs 7−10 and the fitted data in Figure 4 are utilized, as often performed in a conventional analysis, only the aspect ratio L/d may be determined with precision. To further solve the individual parameters of the length L and the diameter d, auxiliary data or observations such as EM images were typically required. Alternatively, we propose here that by fitting the full DLS and DDLS curves using eqs 5 and 6 along with eqs 7−10, it is possible to obtain accurate results on L and d within light scattering experiments. This is crucial in many cases, especially when EM images do not faithfully reproduce the pristine geometrical features in solution. In practice, the (global) fitting is performed simultaneously over data collected at four different scattering angles for both DLS and DDLS experiments, as demonstrated in Figures 2 and 3.

It can be seen from the results gathered in Table 1 that the geometrical features of isolated small rods (for the fast mode) are in excellent agreement in DLS and DDLS experiments. For cylindrical aggregate clusters of the slow mode, the deviations are somewhat larger between the two experiments, which might be attributed to the lack of information on the rotational diffusivity in the DLS (VV) experiment, as discussed previously. Overall, the agreement seems to be quite satisfactory, especially when compared to the results of other independent analyses to be presented shortly.

The data reported in Figure 2b or 3b, in principle, also provide a way to evaluate the volume fraction of the individual species (i.e., isolated small rod vs cylindrical aggregate cluster) by making appropriate assumptions about their contributions to the scattering intensity. Herein, we assume that the reflective index contrast between polymer and solvent is the same for the two species. First, the hydrodynamic radius of rod-like particles can be obtained by $R_h = L/[2\delta - 0.19 - (8.24/\delta) + (12/\delta^2)]$, where $\delta = \ln(2L/d)$.[48] The scattering intensity then scales with the square (for Gaussian coils)[50] or cubic (for solid spheres)[51] of the hydrodynamic radius, $R_{h,i}$. In the former case, for example, the volume fraction may be determined by $R_{h,i}^2$ as

$$W_i = \frac{w_i/R_{h,i}^2}{\sum_i (w_i/R_{h,i}^2)} \quad (11)$$

where w_i is the (intensity-weighed) DLS area associated with the ith mode, and $R_{h,i}$ is the associated hydrodynamic radius. Noticing that the (mean) results seem to be insensitive to either assumption of the molecular type, the predictions from eq 11 are provided in Table 1 to shed light on the relative partition of the two species as well as on the effect of polymer concentration. Accordingly, it appears that increasing polymer concentration has an effect of reducing the volume fraction of isolated small rods.

3.3. Structural Features of pBTTT-C_{14} Aggregates in Toluene. Besides a slight difference in the volume fraction of isolated small rods, the information gathered in Table 1 indicates that the geometrical features of pBTTT-C_{14}/toluene solutions are basically no different in the range of polymer concentrations investigated. Figure 5 presents the SAXS intensity normalized by the corresponding polymer concentration. The overall SAXS profile differs for the 0.5 mg/mL solution primarily in the low-q (<0.1 nm^{-1}) regime. Using the geometrical features obtained in prior DLS/DDLS analyses to locate the pertinent range of q in the SAXS profile, it becomes clear that a notable upturn at low q associated with the 0.9 and 1.2 mg/mL sample solutions is an indication of the dominance of aggregate cluster species to the scattering intensity. At high q, on the other hand, the profile clearly marks the rod-like feature $I(q) \sim q^{-1}$ of isolated small rods, with the cross-sectional feature $I(q) \sim q^{-4}$ at still higher q being obscured within the present SAXS resolution limit. In the intermediate q range, the SAXS profile overlaps ideally at all three concentrations. Therefore, this range of SAXS profile may be utilized for a detailed structural analysis of mixing isolated small rods and cylindrical aggregate clusters.

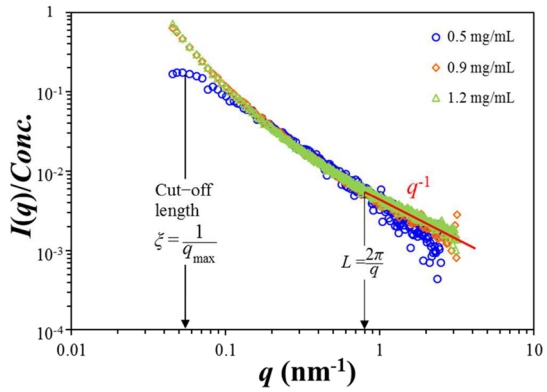

Figure 5. SAXS intensity profiles normalized by the polymer concentration for pBTTT-C_{14}/toluene solutions at three different concentrations, where the vertical lines mark the crossovers that can be used to estimate the cutoff length (ζ) (see a later definition) as well as the length (L) of isolated small rods.

The strategy of structural analysis is to combine SLS and SAXS profiles for a simultaneous revelation of the (mesoscale) geometrical feature, the (interior) fractal structure, and the (nanoscale) packing units of pBTTT-C_{14} aggregate clusters, along with the isolated small-rod species that is coexistent with the aggregate clusters. It can be seen from Figure 6 that the combined scattering profiles cover length scales approximately from 0.3 to 300 nm, and therefore different physical models are required to capture various contributions to the total scattering intensity, as detailed below.

In the low-q region, a Guinier plateau of the SLS data, $I_{SLS}(q)$, is clearly observable at all concentrations. According to prior DLS/DDLS analyses, $I_{SLS}(q)$ in this regime may be described by the form factor of randomly oriented cylinders (with radius R and length L), $P_{cyl}(q)$:

DOI: 10.1021/acs.macromol.7b00790
Macromolecules 2017, 50, 5498−5509

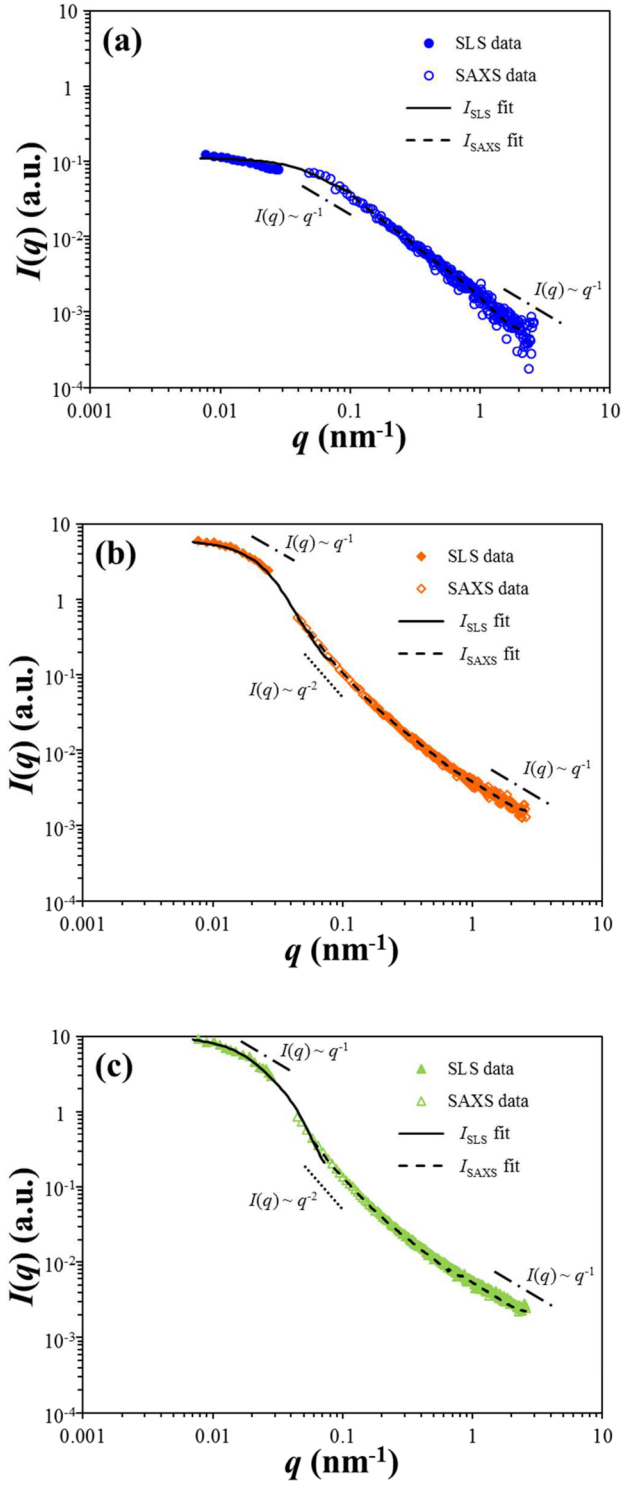

Figure 6. Combined SLS and SAXS intensity profiles for (a) 0.5, (b) 0.9, and (c) 1.2 mg/mL pBTTT-C_{14}/toluene solutions at T = 25.0 °C. At low q (<0.055 nm^{-1}), the $I_{SLS}(q)$ data are described by a cylindrical form factor (continuous line); at higher q (for q > 0.055 nm^{-1}), the dashed line represents the fit of $I_{SAXS}(q)$ data using eqs 13 and 14.

$$P_{cyl}(q) = \int_0^{\pi/2} \left(\frac{\sin\left(\frac{qL}{2}\cos\varphi\right) 2J_1(qR\sin\varphi)}{\left(\frac{qL}{2}\cos\varphi\right)(qR\sin\varphi)} \right)^2 \sin\varphi \, d\varphi \quad (12)$$

In this expression, further corrected by a Schulz–Zimm distribution in length, $I_{SLS}(q) = n\Delta\rho^2 V^2 P_{cyl,1}(q)$, where $J_1(x)$ is the Bessel function of the first kind, n denotes the number density, $\Delta\rho$ is scattering length density contrast, and V is the volume of a cylindrical aggregate cluster. Here, n, $\Delta\rho$, and V are treated as adjustable parameters, which have no effect on the q dependence of the form factor for determining the two geometrical parameters L and R. Note that the combination of $I_{SLS}(q)$ and $I_{SAXS}(q)$ requires a smooth transit between the two sets of data and, furthermore, that the resulting geometrical parameters fitted from $I_{SLS}(q)$ should well reproduce prior DLS/DDLS analyses. From the results gathered in Table 2 and the overall fitting shown in Figure 6, these conditions have been reasonably fulfilled.

In the intermediate-q region, the scattering intensity exhibits a clear q^{-2} dependence for the two more concentrated samples, indicative of the fractal dimension of an aggregate cluster. This is the regime where the fitted $I_{SLS}(q)$ and $I_{SAXS}(q)$ overlap, and physically it means that the fractal structure constitutes an interior (Gaussian) network within a cylindrical aggregate cluster. Followed by a nearly q^{-1} dependence in the high-q region of $I_{SAXS}(q)$, the total scattering intensity may be described by the contributions of rod-like packing units of the aggregate cluster along with isolated small rods. Assuming that the packing unit is basically no different from the isolated rod species, the following expression is utilized to describe the full range of SAXS data:

$$I_{SAXS}(q) \sim P_{cyl,2,tol}(q)S(q) + n_{isolated}\Delta\rho_{isolated}{}^2 V_{isolated}{}^2 P_{cyl,2,tol}(q) \quad (13)$$

In eq 13, the first term describes the contributions from small-rod packing units (i.e., the form factor) as well as the fractal structure (i.e., the structure factor) that embodies them within an aggregate cluster. A rather general structure factor $S(q)$ for this purpose is

$$S(q) = 1 + \frac{D_f \Gamma(D_f - 1)\sin(D_f - 1)\tan^{-1}(q\zeta)}{(qR_e)^{D_f}[1 + (q\zeta)^{-2}]^{(D_f-1)/2}} \quad (14)$$

where D_f is the fractal dimension; ξ is the cutoff length marking the boundary of an aggregate cluster or, more generally, the (colloidal) network system beyond which the mass distribution is no longer described by the fractal law, and thus it is expected to bear magnitude comparable with the mean size of pBTTT-C_{14} aggregate clusters; R_e is expected to reflect the dimension of the packing units.

The second term in eq 13 represents the contribution from isolated small rods, where $n_{isolated}$ denotes the number density of isolated small rods, $\Delta\rho_{isolated}$ is scattering length density contrast between pBTTT-C_{14} and the solvent medium, and $V_{isolated}$ is the volume of an isolated small rod. The theoretical scattering length density (SLD) of pBTTT-C_{14} is evaluated using the NIST SLD calculator along with previously published molecular formula of the pBTTT-C_{14} monomeric unit, $C_{42}H_{62}S_4$, and a density of 1.1 g/cm^3;[13,52] the SLDs of pBTTT-C_{14} and the two solvents investigated are $\rho_{pBTTT\text{-}C14}$ = 10.5 × 10^{-6} Å^{-2}, ρ_T = 8.4 × 10^{-6} Å^{-2}, and ρ_{CB} = 9.9 × 10^{-6} Å^{-2}. The theoretical fits superimposed on the original SAXS data are presented in Figure 6, with the fitted geometrical parameters provided in Table 2.

Comparing the geometrical features provided in Tables 1 and 2 for the two main species in pBTTT-C_{14}/toluene solutions reveals close agreement between the (dynamic) DLS/DDLS

DOI: 10.1021/acs.macromol.7b00790
Macromolecules 2017, 50, 5498–5509

Table 2. Structural Parameters Extracted from the SLS/SAXS Analyses of pBTTT-C_{14}/Toluene Solutions

method		concentration (mg/mL) 0.5	0.9	1.2
SLS and SAXS	length of cylindrical aggregate cluster (L) [nm]	153 ± 14	251 ± 20	310 ± 16
	radius of cylindrical aggregate cluster (R) [nm]	23	42	56
	radius of gyration $R_{g,cyl}$ [nm][a]	55	94	115
	length of isolated small rod (L) [nm]	7.1 ± 0.2	7.7 ± 0.2	10.5 ± 0.2
	radius of isolated small rod (R) [nm]	2.2 ± 0.1	2.3 ± 0.1	2.1 ± 0.1
	fractal dimension (D_f)	1.98 ± 0.02	2.56 ± 0.02	2.66 ± 0.02
	cutoff length (ξ) [nm]	11.3 ± 0.1	19.2 ± 0.2	20.5 ± 0.3
	effective radius of packing unit (R_e) [nm]	0.51 ± 0.02	0.65 ± 0.02	0.70 ± 0.03
	radius of gyration $R_g_S(q)$ [nm][b]	27	58	64
	$n_{isolated}$ [10^{14} cm^{-3}]	8.57	5.36	3.89

[a]Calculated from the relation $R_{g,cyl} = L^2/12 + d^2/2$. [b]Calculated from the relation $R_g_S(q) = [D_f(D_f + 1)]^{0.5}\xi$.

and (static) SLS/SAXS analyses. Several features should be further noted. First, the fractal dimension in Table 2 indicates increasingly more compact aggregate clusters fostered at higher pBTTT-C_{14} concentrations. Second, the concentration-dependent number density of isolated small rods exhibits the same trend as previously found in the DLS/DDLS analyses. Third, Wang et al.[53] previously reported on the self-assembling of pBTTT-C_{14} into isolated one-dimensional (1-D) fibers in chloroform, and they assigned a thickness of 4−6 nm to the 1-D fibers, which compares favorably with the diameter of isolated small rods in Tables 1 and 2.

3.4. DLS/DDLS Features of pBTTT-C_{14} Aggregates in Chlorobenzene. The DDLS feature in Figure 1b and the EM images in Figure 10b all indicate that pBTTT-C_{14} clusters are basically isotropic (spherical) in chlorobenzene. Figure 7 shows

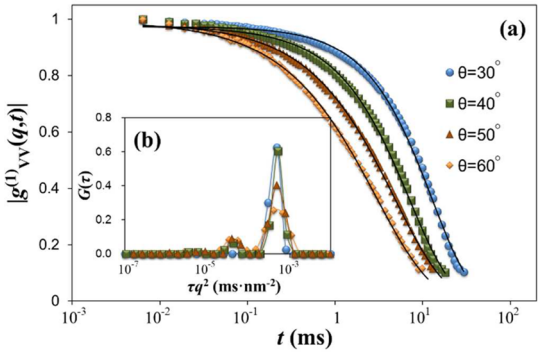

Figure 7. (a) Angular dependences of the field autocorrelation function, $|g^{(1)}_{VV}(q,t)|$ and (b) relaxation time distributions, $G(\tau)$, retrieved from CONTIN as a function of τq^2 for the 0.9 mg/mL pBTTT-C_{14}/chlorobenzene solution. The fast mode corresponds to isolated small rods, and the slow mode corresponds to spherical aggregate clusters. The solid lines are nonlinear least-squares fits using eq 15.

the field autocorrelation function, $|g^{(1)}_{VV}(q,t)|$, and the relaxation time distribution function, $G(\tau)$, extracted from CONTIN for a representative pBTTT-C_{14}/chlorobenzene solution at 0.9 mg/mL and T = 25.0 °C. The CONTIN analysis in Figure 7b reveals two distinct modes (i.e., the fast and slow modes). The field autocorrelation functions are qualitatively similar at two other concentrations, as shown in Figure S6. Figure 8 shows that although the mean decay rates, $\langle\Gamma\rangle$, for the two modes are both linearly dependent on q^2, they are of distinct natures Notably, the extrapolation to q = 0 for

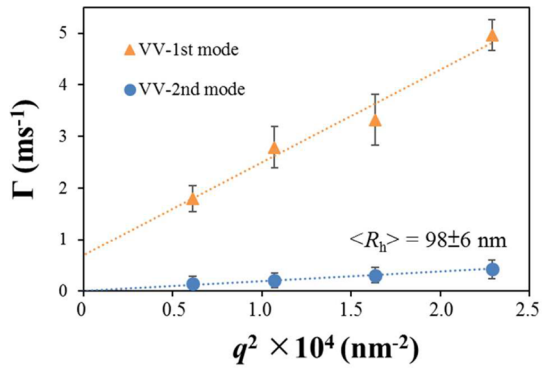

Figure 8. Mean decay rates, $\langle\Gamma\rangle$, as a function of q^2 for the 0.9 mg/mL pBTTT-C_{14}/chlorobenzene solution, where the dotted lines denote the results of linear regression.

the fast mode does not pass through the origin, indicative of the formation of small rod species. In contrast, the slow mode displays the usual diffusive attribute with the extrapolation passing through the origin. Along with the central observations in DDLS and EM characterizations noted above, the slow mode may be attributed to the motion of *spherical* aggregate clusters. Similar features can be noted in Figure S7 for the other concentrations. Thus, the coexistence of isolated small rods and spherical aggregate clusters in the pBTTT-C_{14}/chlorobenzene solutions seems evident. In this case, the mean hydrodynamic radius $\langle R_h\rangle$ of a spherical aggregate cluster can be readily estimated from the Stokes−Einstein relation, $\langle R_h\rangle = k_BT/6\pi\eta\langle D\rangle$, as indicated in Figure 8.

According to the features in Figure 8, the field autocorrelation function may be expressed as

$$|g^{(1)}_{VV}(q,t)| = A\exp\{-[(D_{T,fast}q^2 + 6D_{R,fast})t]^{\alpha}\} + (1-A)\exp\{-[(D_{T,slow}q^2)t]^{\beta}\} \quad (15)$$

This formula, along with eqs 7−10, may be utilized to obtain the best fits of the geometrical parameters of L (length of an isolated small rod), d (diameter of an isolated small rod), and $\langle R_h\rangle$ (hydrodynamic radius of a spherical aggregate cluster), in a way as described earlier. The full-curve fitting is shown in Figure 7a (solid lines), and the parameter values are gathered in Table 3. Similarly, the decay time distributions of the two individual modes shown in Figure 7b can be used for a rough estimate of the volume fraction of each species, as provided in the same table. It is of interest to note that while the shapes of aggregate clusters differ substantially, the properties of isolated

DOI: 10.1021/acs.macromol.7b00790
Macromolecules 2017, 50, 5498−5509

Table 3. Parameter Values Extracted from the DLS Analysis of pBTTT-C_{14}/Chlorobenzene Solutions

			concentration (mg/mL)		
method			0.5	0.9	1.2
DLS	isolated small rod	length (L) [nm]	12.9 ± 7.1	12.9 ± 7.1	11.6 ± 1.0
		diameter (d) [nm]	6.0 ± 3.9	6.0 ± 3.9	5.3 ± 0.6
		stretch exponent (α)	0.32 ± 0.03	0.38 ± 0.02	0.52 ± 0.04
		aspect ratio	2.2	2.2	2.2
	spherical aggregate cluster	hydrodynamic radius ($\langle R_h \rangle$) [nm]	63 ± 9	98 ± 6	132 ± 13
		stretch exponent (β)	0.61 ± 0.01	0.83 ± 0.01	0.82 ± 0.02
	$W_{\text{isolated small rod}}$		0.95	0.86	0.79

small rods listed in Tables 1 and 3 for the two solvent media differ only slightly.

Using intrinsic viscosity data, Zhao et al.[15] have previously suggested that pBTTT-C_{14} chains in dilute CB solutions (1−4 mg/mL) adopt a random-coil but not rigid-rod conformation. With the (single-angular) DLS analysis, Wang et al.[18,19] subsequently reported on the coexistence of two distinct R_h for pBTTT-C_{12}/o-DCB solutions at 69.0−87.7 and 7.1−11.3 nm, respectively. They attributed the larger R_h to aggregates and the smaller one to single pBTTT-C_{12} chains, based on the geometrical features of pBTTT-C_{14} in CB as had been reported earlier by Zhao et al.[15] If a similar assumption is made, our DLS data on pBTTT-C_{14}/CB solutions would lead to a similar conclusion with regard to the sizes of the individual species. However, given that our (multiangular) DLS analysis clearly suggests that the fast mode represents anisotropic molecules, the geometrical features reported in Table 3 should be more credible. For comparison, dilute solutions that foster (isotropic) interchain aggregates have been reported in previous FCS[29] and DLS[35] studies on another conjugated polymer, poly[2-methoxy-5-(2-ethylhexyloxy)-1,4-phenylenevinylene] (MEH-PPV).

3.5. Structural Features of pBTTT-C_{14} Aggregates in Chlorobenzene. Similar to the previous analyses performed on pBTTT-C_{14}/toluene solutions, Figure 9 shows how combined SLS and SAXS profiles can be employed to reveal the static structural features of pBTTT-C_{14}/chlorobenzene solutions. The major difference consists in that the form factor of spheres (with radius R), $P_{sph}(q)$, is considered (with a Schulz−Zimm distribution for the radius) to reflect the isotropic aggregate clusters previously revealed in the DDLS/DLS analyses:

$$P_{sph}(q) = \left(3\frac{\sin(qR) - qR\cos(qR)}{(qR)^3}\right)^2 \quad (16)$$

and thus $I_{SLS}(q) = n\Delta\rho^2V^2P_{sph}(q)$.

For the SAXS data, it can be seen that in the intermediate-q region the scattering intensity exhibits either q^{-2} (0.9 mg/mL) or q^{-3} (1.2 mg/mL) dependence. This regime, usually known as the Porod regime, marks the transit from the surface feature to the aggregate interior and is described by the scattering law $I(q) \sim q^{-4}$. The deviations from the previous scaling law, especially for the 0.9 mg/mL solution, could be indicative of a rough cluster surface[54] as well as the effect of polydispersity in aggregate size. In the high-q region, the common feature of a q^{-1} dependence reflects the 1-D nature of isolated small rods. Thus, the major part of the $I_{SAXS}(q)$ data reflects the fractal structure of the aggregate cluster, its packing units, and coexistent isolated small rods, as described by eq 13.

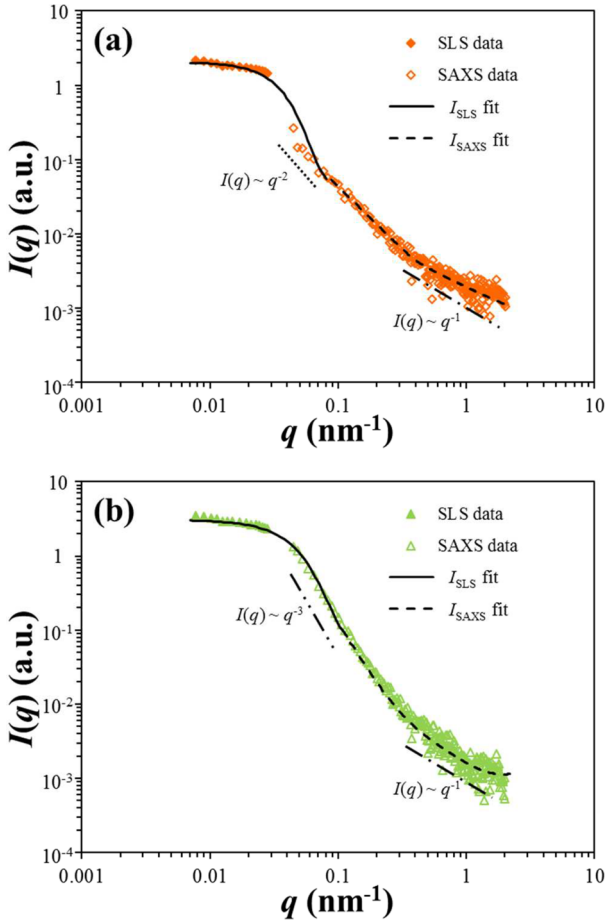

Figure 9. Combined SLS and SAXS intensity profiles for (a) 0.9 and (b) 1.2 mg/mL pBTTT-C_{14}/chlorobenzene solutions at T = 25.0 °C. At low q (<0.1 nm^{-1}), the data are described by spherical form factor (solid line), and the dashed line for q > 0.1 nm^{-1} represents the fit using eq 13.

The overall fits superimposed on the original SLS/SAXS data are presented in Figure 9, with the geometrical parameters provided in Table 4. Comparing the geometrical features in Tables 3 and 4 reveals generally close agreement between the (dynamic) DLS and (static) SLS/SAXS analyses. In particular, the ρ ratio, which describes the structural compactness of the aggregate cluster, is in good agreement with the theoretical prediction for colloidal spheres, i.e., ρ = 0.775. Despite a similar geometrical feature, it seems that the number density of isolated small rods, $n_{isolated}$, is substantially higher in pBTTT-C_{14}/chlorobenzene solutions than in the counterpart pBTTT-C_{14}/toluene solutions. The simulation results discussed shortly

DOI: 10.1021/acs.macromol.7b00790
Macromolecules 2017, 50, 5498−5509

Table 4. Structural Parameters Extracted from the SLS/SAXS Analyses of pBTTT-C_{14}/Chlorobenzene Solutions

		concentration (mg/mL)		
method		0.5	0.9	1.2
SLS and SAXS	radius of spherical aggregate cluster (R) [nm]	–	69 ± 5	82 ± 7
	length of isolated small rod (L) [nm]	–	8.2 ± 0.3	10.3 ± 0.1
	radius of isolated small rod (R) [nm]	–	1.5 ± 0.2	2.0 ± 0.2
	fractal dimension (D_f)	–	2.23 ± 0.01	2.43 ± 0.03
	cutoff length (ξ) [nm]	–	24.9 ± 0.2	30.3 ± 0.4
	effective radius of packing unit (R_e) [nm]	–	0.51 ± 0.01	0.67 ± 0.02
	radius of gyration R_g $S(q)$ [nm][a]	–	65	86
	ρ ratio[b]	–	0.66–0.70	0.62–0.65
	$n_{isolated}$ [10^{16} cm^{-3}]	–	13.1	2.2

[a]Calculated from the relation R_g $S(q) = [D_f(D_f + 1)]^{0.5}\xi$. [b]Calculated from the relation $\rho = R_g S(q)/\langle R_h \rangle$.

provide some insight into the major disparities between the two solution systems.

3.6. Thin-Film Microscopy Morphologies. Complementary to prior DLS/DDLS/SLS/SAXS analyses, Figure 10

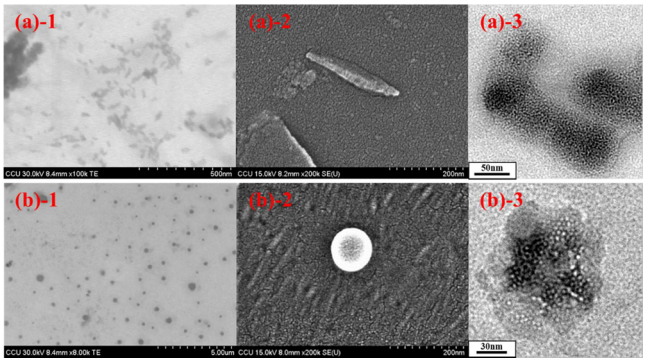

Figure 10. Morphologies of drop-casting thin films produced from pBTTT-C_{14} solutions at 0.9 mg/mL and T = 25.0 °C using the solvent media of (a) toluene and (b) chlorobenzene, for images taken from (1) STEM, (2) SEM, and (3) TEM measurements.

presents various EM (i.e., STEM, SEM, and TEM) morphologies of drop-casting thin films produced from representative pBTTT-C_{14} solutions at c = 0.9 mg/mL. A fast drying of the thin-film samples before the EM images were taken helps preserve the aggregate features in solution state.[55] The results clearly confirm the anisotropic feature of pBTTT-C_{14} aggregate clusters fostered in toluene, in contrast with the isotropic ones in chlorobenzene. The EM sizes of pBTTT-C_{14} clusters are also in good agreement with prior scattering analyses. Similarly, for (unannealed) thin films spin-coated from pBTTT-C_{12}/o-DCB solutions, Wang et al.[18] have previously reported on sphere-like (or dot-like) features in TEM imaging, which compared favorably with the nodule-featured (or particle-like) topography of as-cast pBTTT-C_{12} films as had been revealed earlier by AFM.[2,24]

In summary, we show that combined DLS, DDLS, SLS, and SAXS analyses and EM imaging lead to a clear revelation of the multiscale features of pBTTT-C_{14} aggregate clusters fostered in two slightly different aromatic solvents, as pictorially summarized in Figure 11. An interesting feature is that similar

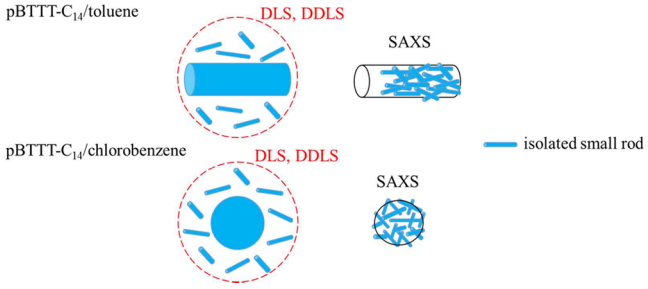

Figure 11. Schematic illustrations of a hierarchy of structural features of pBTTT-C_{14} clusters incubated in two slightly different aromatic solvents.

isolated rods seem to coexist with the aggregate clusters, which assume distinct shapes in the two solvent media. Previously, Wang et al.[18,19] suggested that when the solubility parameters of the solvent and the polymer are close to each other, pBTTT-C_{14} tends to form nanofibrils which, in turn, self-assemble into isolated 1-D fibers similar to what had been reported earlier by Wang et al.[53] According to the Hansen solubility parameters provided in Table 5, this prediction would better apply to

Table 5. Hansen Solubility Parameters

solvent or polymer	solubility parameter[a] ($MPa^{0.5}$)
pBTTT-C_{14}	18.22
toluene	18.16
chlorobenzene	19.58

[a]The results were taken from the estimation made in ref 21.

pBTTT-C_{14}/toluene than to pBTTT-C_{14}/chlorobenzene solution. Still, the AMD simulations discussed next seem to suggest that other physics is at work for this phenomenon.

3.7. Single-Chain and Small-Aggregate Features from AMD Simulations. To gain molecule-level insights into the two pBTTT-C_{14} solution systems investigated, we have performed a series of AMD simulations using rigorously determined force field and reliable system preparation scheme, as detailed in Supporting Information (sections S2 and S3). The static and dynamic properties of single pBTTT-C_{14} chains, each consisting of 12 monomer units, and their five-chain aggregates in toluene and chlorobenzene, respectively, are investigated in detail. Figure 12 illustrates that the five-chain aggregates were initially arranged into a perfect π–π stacking; as the time evolved, while the aggregate sustains a highly anisotropic (π–π stacking) structure in toluene, it becomes notably disrupted and progressively disperses into separate units in chlorobenzene. A detailed structural analysis based on the interchain order parameter (see section S4) also indicates the persistence or collapse of π–π stacking in the same process. These observations clearly suggest that although rod-like aggregates may prevail in both solvent media, only in the poorer solvent (as judged by the visual solubility of pBTTT-C_{14}) toluene would it be able to sustain the compact π–π stacking structure in solution. The UV–vis absorption spectra provided in Figure S1 appear to lend support to this assertion.

DOI: 10.1021/acs.macromol.7b00790
Macromolecules 2017, 50, 5498–5509

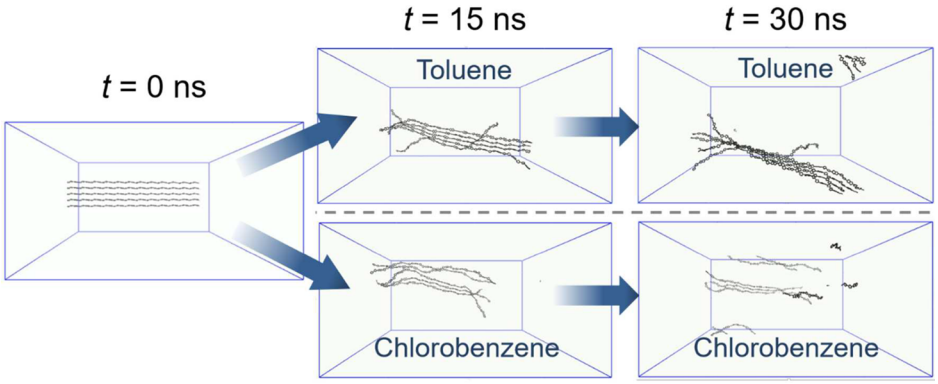

Figure 12. Time evolutions of five-chain aggregate morphologies in toluene (top) and chlorobenzene (bottom); only atoms in the conjugated backbone are shown for clarity.

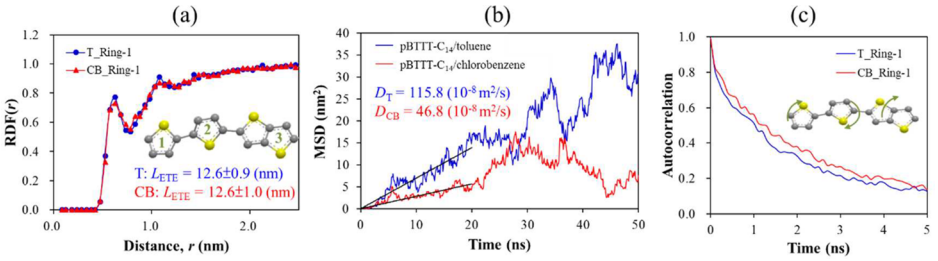

Figure 13. Analyses of static structural features and dynamic properties of a single pBTTT-C_{14} chain in toluene (blue) and chlorobenzene (red) media: (a) the radial distribution function (RDF) of the solvent−thiophene pair and the mean end-to-end distance of a full chain, where the RDF of the solvent−thienothiophene pair is compared in Figure S11; (b) the mean-square displacement (MSD) and corresponding center-of-mass diffusivity; (c) the relaxation dynamics of backbone torsional conformation, as described in section S5.

Regarding the DLS/DDLS analyses of the fast-mode properties, it now seems that the isolated small-rod species identified in both solvent media should be fundamentally different in the bolstering interaction forces. In chlorobenzene, pBTTT-C_{14} aggregates may have been sustained by the usual (isotropic) van der Waals forces, resulting in less "anisotropic persistence" unlike those fostered in toluene, wherein strong and highly ordered $\pi-\pi$ interaction is at work. As a result, the subsequent packing into larger aggregate clusters appears to follow distinct pathways and result in notably different geometrical shapes. For instance, it could be that the (semiflexible) rods formed in chlorobenzene naturally favor an isotropic packing into spherical aggregate clusters. In future work, to capture the underlying growth process, coarse-grained simulations capable of simulating a larger number of chains as well as longer chain lengths will be necessary.

To gain deeper insight into the contrasting aggregation features noted above, we have also performed detailed static (structure) and dynamic (relaxation) analyses of single pBTTT-C_{14} chain in either solvent medium. Figure 13 reveals that static structural features (Figure 13a), such as the mean end-to-end distance of a pBTTT-C_{14} chain and the radial distribution function (RDF) of the solvent−thiophene pair, are basically no different in the two solvent media. From a dynamic perspective, however, the pBTTT-C_{14} chain in toluene is found to possess a considerably higher center-of-mass diffusivity and, in particular, more rapid relaxation of the backbone torsional conformation than in chlorobenzene, as shown in Figure 13b,c. Obviously, the disparity cannot be explained by the difference in solvent viscosity.

The effect of the relatively fast dynamics in pBTTT-C_{14}/toluene solution is twofold. A higher chain mobility increases the encounter probability of pBTTT-C_{14} chains; furthermore, the rapid relaxation of the backbone torsional conformation greatly facilitates pBTTT-C_{14} chains to search for favorable mutual alignment in order to form $\pi-\pi$ stacking. In contrast, the relatively sluggish dynamics of pBTTT-C_{14} chains in chlorobenzene results in more erratic and, hence, looser aggregate packing through isotropic van der Waals forces. Dynamic properties—but not static ones, as usually accounted for by the Hansen solubility parameters—having a major influence on the solvation behavior of pBTTT-C_{14} chains may be traced back to the sophisticated polymer−solvent interactions in the proximity of the pBTTT-C_{14} backbone, akin to what have recently been revealed for fullerene[56,57] and conjugated polymer[58,59] solutions.

4. CONCLUSION

Using a comprehensive combination of dynamic (DLS/DDLS) and static (SLS/SAXS) scattering analysis schemes along with electronic microscopy (STEM/SEM/TEM) imaging techniques, we show that the use of two slightly different aromatic solvents, toluene and chlorobenzene, can lead to substantial differences in the multiscale aggregate features of pBTTT-C_{14} in solution and thin film. Whereas the aggregate clusters assume an anisotropic, cylindrical shape (aspect ratio ~3) in toluene, they are nearly isotropic, sphere-like in chlorobenzene, with mean sizes of a few hundred nanometers. In both solvent media, a certain fraction of isolated rod-like species (~10 nm in length; aspect ratio ~2) coexistent with the aggregate clusters have been clearly identified in both dynamic (DLS) and static (SAXS) analyses. The present study suggests, however, that they are most likely small (anisotropic) aggregates (see, for instance, the discussion in section S6), instead of isolated

DOI: 10.1021/acs.macromol.7b00790
Macromolecules 2017, 50, 5498−5509

chains as previously suggested. Similar rod-like species are suggested to serve as the packing unit of the aggregate clusters. Accurate AMD simulations for both one- and five-chain aggregate systems clearly reveal that the solvent media impact the aggregate properties primarily through the dynamic relaxation of the backbone conformation of pBTTT-C_{14}. The consequent disparities in the bolstering interaction force (van der Waals vs $\pi-\pi$) and, hence, the "anisotropic persistence" of the fundamental packing units could be responsible for the distinct mesoscale aggregate features revealed herein for the two solvent media. It remains unclear whether the (semi-flexible) rods with less such persistence in the chlorobenzene medium would naturally favor an isotropic packing into spherical aggregate clusters, whereas the relatively rigid rods fostered in toluene are especially effective for internal energy reduction through an anisotropic packing into cylindrical aggregate clusters. Overall, the present study implies that the mesoscale/nanoscale aggregation properties of pBTTT-C_{14} in solution and thin film can be effectively controlled by exploiting different solvent media. Along with the recent reports on the morphological developments of the pBTTT-C_n series during thin-film formation, the knowledge should greatly facilitate the current applications with organic photovoltaic cells and thin-film transistors.

■ ASSOCIATED CONTENT

Supporting Information

The Supporting Information is available free of charge on the ACS Publications website at DOI: 10.1021/acs.macromol.7b00790.

UV−vis absorption spectra of two representative dilute pBTTT-C_{14}solutions, compilation of DLS/DDLS data and analyses, description and validation of the force field for AMD simulations, simulation methodology and analysis schemes of interchain order parameter, RDF, and torsional conformation relaxation, computational insight into light scattering analysis (PDF)

■ AUTHOR INFORMATION

Corresponding Author

*E-mail: chmcch@ccu.edu.tw (C.C.H.).

ORCID

Chi C. Hua: 0000-0003-3398-2576

Notes

The authors declare no competing financial interest.

■ ACKNOWLEDGMENTS

This research was supported by the Ministry of Science and Technology of ROC (MOST 103-2221-E-194-059-MY3). We acknowledge the NSRRC of ROC for providing beamtimes and facilitating the SAXS experiments and the resources provided by the National Center for High-Performance Computing of ROC.

■ REFERENCES

(1) Hamadani, B. H.; Gundlach, D. J.; McCulloch, I.; Heeney, M. Undoped Polythiophene Field-Effect Transistors with Mobility of 1 $cm^2v^{-1}s^{-1}$. *Appl. Phys. Lett.* **2007**, *91*, 243512.

(2) McCulloch, I.; Heeney, M.; Bailey, C.; Genevicius, K.; MacDonald, I.; Shkunov, M.; Sparrowe, D.; Tierney, S.; Wagner, R.; Zhang, W.; et al. Liquid-Crystalline Semiconducting Polymers with High Charge-Carrier Mobility. *Nat. Mater.* **2006**, *5*, 328−333.

(3) DeLongchamp, D. M.; Kline, R. J.; Jung, Y.; Lin, E. K.; Fischer, D. A.; Gundlach, D. J.; Cotts, S. K.; Moad, A. J.; Richter, L. J.; Toney, M. F.; et al. Molecular Basis of Mesophase Ordering in a Thiophene-Based Copolymer. *Macromolecules* **2008**, *41*, 5709−5715.

(4) DeLongchamp, D. M.; Kline, R. J.; Lin, E. K.; Fischer, D. A.; Richter, L. J.; Lucas, L. A.; Heeney, M.; McCulloch, I.; Northrup, J. E. High Carrier Mobility Polythiophene Thin Films: Structure Determination by Experiment and Theory. *Adv. Mater.* **2007**, *19*, 833−837.

(5) Chabinyc, M. L.; Toney, M. F.; Kline, R. J.; McCulloch, I.; Heeney, M. X-ray Scattering Study of Thin Films of Poly(2,5-bis(3-alkylthiophen-2-yl)thieno[3,2-b]thiophene). *J. Am. Chem. Soc.* **2007**, *129*, 3226−3237.

(6) Lee, J. K.; Ma, W. L.; Brabec, C. J.; Yuen, J.; Moon, J. S.; Kim, J. Y.; Lee, K.; Bazan, G. C.; Heeger, A. J. Processing Additives for Improved Efficiency from Bulk Heterojunction Solar Cells. *J. Am. Chem. Soc.* **2008**, *130*, 3619−3623.

(7) Hoven, C. V.; Dang, X.-D.; Coffin, R. C.; Peet, J.; Nguyen, T.-Q.; Bazan, G. C. Improved Performance of Polymer Bulk Heterojunction Solar Cells through the Reduction of Phase Separation via Solvent Additives. *Adv. Mater.* **2010**, *22*, E63−E66.

(8) Merlo, J. A.; Frisbie, C. D. Field Effect Conductance of Conducting Polymer Nanofibers. *J. Polym. Sci., Part B: Polym. Phys.* **2003**, *41*, 2674−2680.

(9) Kline, R. J.; DeLongchamp, D. M.; Fischer, D. A.; Lin, E. K.; Richter, L. J.; Chabinyc, M. L.; Toney, M. F.; Heeney, M.; McCulloch, I. Critical Role of Side-Chain Attachment Density on the Order and Device Performance of Polythiophenes. *Macromolecules* **2007**, *40*, 7960−7965.

(10) DeLongchamp, D. M.; Kline, R. J.; Jung, Y.; Germack, D. S.; Lin, E. K.; Moad, A. J.; Richter, L. J.; Toney, M. F.; Heeney, M.; McCulloch, I. Controlling the Orientation of Terraced Nanoscale "Ribbons" of a Poly(thiophene) Semiconductor. *ACS Nano* **2009**, *3*, 780−787.

(11) Northrup, J. E. Atomic and Electronic Structure of Polymer Organic Semiconductors: P3HT, PQT, and PBTTT. *Phys. Rev. B: Condens. Matter Mater. Phys.* **2007**, *76*, 245202.

(12) Brocorens, P.; Van Vooren, A.; Chabinyc, M. L.; Toney, M. F.; Shkunov, M.; Heeney, M.; McCulloch, I.; Cornil, J.; Lazzaroni, R. Solid-State Supramolecular Organization of Polythiophene Chains Containing Thienothiophene Units. *Adv. Mater.* **2009**, *21*, 1193−1198.

(13) Cho, E.; Risko, C.; Kim, D.; Gysel, R.; Cates Miller, N.; Breiby, D. W.; McGehee, M. D.; Toney, M. F.; Kline, R. J.; Bredas, J.-L. Three-Dimensional Packing Structure and Electronic Properties of Biaxially Oriented Poly(2,5-bis(3-alkylthiophene-2-yl)thieno[3,2-b]-thiophene) Films. *J. Am. Chem. Soc.* **2012**, *134*, 6177−6190.

(14) Hamilton, R.; Bailey, C.; Duffy, W.; Heeney, M.; Shkunov, M.; Sparrowe, D.; Tierney, S.; McCulloch, I.; Kline, R. J.; DeLongchamp, D. M.; et al. The Influence of Molecular Weight on the Microstructure and Thin Film Transistor Characteristics of PBTTT Polymers. *Proc. SPIE* **2006**, *6336*, 633611.

(15) Zhao, L.-H.; Png, R.-Q.; Zhuo, J.-M.; Wong, L.-Y.; Tang, J.-C.; Su, Y.-S.; Chua, L.-L. Role of Borderline Solvents to Induce Pronounced Extended-Chain Lamellar Order in π-Stackable Polymers. *Macromolecules* **2011**, *44*, 9692−9702.

(16) Gasperini, A.; Sivula, K. Effects of Molecular Weight on Microstructure and Carrier Transport in a Semicrystalline Poly(thieno)thiophene. *Macromolecules* **2013**, *46*, 9349−9358.

(17) Liu, J.; Mikhaylov, I. A.; Zou, J.; Osaka, I.; Masunov, A. E.; McCullough, R. D.; Zhai, L. Insight into How Molecular Structures of Thiophene-Based Conjugated Polymers Affect Crystallization Behaviors. *Polymer* **2011**, *52*, 2302−2309.

(18) Wang, H.; Liu, J.; Han, Y. Nano-Fibrils Formation of PBTTT via Adding Alkylthiol into Solutions: Control of Morphology and Crystalline Structure. *Polymer* **2013**, *54*, 948−957.

(19) Wang, H.; Liu, J.; Xu, Y.; Han, Y. Fibrillar Morphology of Derivatives of Poly(3-alkylthiophene)s by Solvent Vapor Annealing: Effects of Conformational Transition and Conjugate Length. *J. Phys. Chem. B* **2013**, *117*, 5996−6006.

DOI: 10.1021/acs.macromol.7b00790
Macromolecules 2017, 50, 5498−5509

(20) Wang, S.; Tang, J.-C.; Zhao, L.-H.; Png, R.-Q.; Wong, L.-Y.; Chia, P.-J.; Chan, H. S. O.; Ho, P. K.-H.; Chua, L.-L. Solvent Effects and Multiple Aggregate States in High-Mobility Organic Field-Effect Transistors Based on Poly(bithiophene-*alt*-thienothiophene). *Appl. Phys. Lett.* **2008**, *93*, 162103.
(21) Gaikwad, A. M.; Khan, Y.; Ostfeld, A. E.; Pandya, S.; Abraham, S.; Arias, A. C. Identifying Orthogonal Solvents for Solution Processed Organic Transistors. *Org. Electron.* **2016**, *30*, 18−29.
(22) Alberga, D.; Mangiatordi, G. F.; Torsi, L.; Lattanzi, G. Effects of Annealing and Residual Solvents on Amorphous P3HT and PBTTT Films. *J. Phys. Chem. C* **2014**, *118*, 8641−8655.
(23) Lee, M. J.; Gupta, D.; Zhao, N.; Heeney, M.; McCulloch, I.; Sirringhaus, H. Anisotropy of Charge Transport in a Uniaxially Aligned and Chain-Extended, High-Mobility, Conjugated Polymer Semiconductor. *Adv. Funct. Mater.* **2011**, *21*, 932−940.
(24) Zhang, Q.; Sun, Y.; Jiao, F.; Zhang, J.; Xu, W.; Zhu, D. Effects of Structural Order in the Pristine State on the Thermoelectric Power-Factor of Doped PBTTT Films. *Synth. Met.* **2012**, *162*, 788−793.
(25) Schuettfort, T.; Watts, B.; Thomsen, L.; Lee, M.; Sirringhaus, H.; McNeill, C. R. Microstructure of Polycrystalline PBTTT Films: Domain Mapping and Structure Formation. *ACS Nano* **2012**, *6*, 1849−1864.
(26) Knaapila, M.; Stepanyan, R.; Torkkeli, M.; Garamus, V. M.; Galbrecht, F.; Nehls, B. S.; Preis, E.; Scherf, U.; Monkman, A. P. Control over Phase Behavior and Solution Structure of Hairy-Rod Polyfluorene by Means of Side-Chain Length and Branching. *Phys. Rev. E* **2008**, *77*, 051803.
(27) Rahman, M. H.; Chen, C.-Y.; Liao, S.-C.; Chen, H.-L.; Tsao, C.-S.; Chen, J.-H.; Liao, J.-L.; Ivanov, V. A.; Chen, S.-A. Segmental Alignment in the Aggregate Domains of Poly(9,9-dioctylfluorene) in Semidilute Solution. *Macromolecules* **2007**, *40*, 6572−6578.
(28) Li, Y.-C.; Chen, C.-Y.; Chang, Y.-X.; Chuang, P.-Y.; Chen, J.-H.; Chen, H.-L.; Hsu, C.-S.; Ivanov, V. A.; Khalatur, P. G.; Chen, S.-A. Scattering Study of the Conformational Structure and Aggregation Behavior of a Conjugated Polymer Solution. *Langmuir* **2009**, *25*, 4668−4677.
(29) Wang, D.; Yuan, Y.; Mardiyati, Y.; Bubeck, C.; Koynov, K. From Single Chains to Aggregates, How Conjugated Polymers Behave in Dilute Solutions. *Macromolecules* **2013**, *46*, 6217−6224.
(30) Newbloom, G. M.; Kim, F. S.; Jenekhe, S. A.; Pozzo, D. C. Mesoscale Morphology and Charge Transport in Colloidal Networks of Poly(3-hexylthiophene). *Macromolecules* **2011**, *44*, 3801−3809.
(31) Keum, J. K.; Xiao, K.; Ivanov, I. N.; Hong, K.; Browning, J. F.; Smith, G. S.; Shao, M.; Littrell, K. C.; Rondinone, A. J.; Andrew Payzant, E.; et al. Solvent Quality-Induced Nucleation and Growth of Parallelepiped Nanorods in Dilute Poly(3-hexylthiophene) (P3HT) Solution and the Impact on the Crystalline Morphology of Solution-Cast Thin Film. *CrystEngComm* **2013**, *15*, 1114−1124.
(32) Huang, Y.; Cheng, H.; Han, C. C. Unimer−Aggregate Equilibrium to Large Scale Association of Regioregular Poly(3-hexylthiophene) in THF Solution. *Macromolecules* **2011**, *44*, 5020−5026.
(33) Huang, Y.; Cheng, H.; Han, C. C. Temperature Induced Structure Evolution of Regioregular Poly(3-hexylthiophene) in Dilute Solution and its Influence on Thin Film Morphology. *Macromolecules* **2010**, *43*, 10031−10037.
(34) Sun, Q.; Park, K.; Dai, L. Liquid Crystalline Polymers for Efficient Bilayer-Bulk-Heterojunction Solar Cells. *J. Phys. Chem. C* **2009**, *113*, 7892−7897.
(35) Wen, Y. H.; Lin, P. C.; Hua, C. C.; Chen, S. A. Dynamic Structure Factor for Large Aggregate Clusters with Internal Motions: A Self-Consistent Light-Scattering Study on Conjugated Polymer Solutions. *J. Phys. Chem. B* **2011**, *115*, 14369−14380.
(36) Guo, R. H.; Hsu, C. H.; Hua, C. C.; Chen, S. A. Colloidal Aggregate and Gel Incubated by Amorphous Conjugated Polymer in Hybrid-Solvent Medium. *J. Phys. Chem. B* **2015**, *119*, 3320−3331.
(37) Siegert, A. J. F. Report No. 475; MIT Radiation Laboratory, 1943.
(38) Provencher, S. W. A Constrained Regularization Method for Inverting Data Represented by Linear Algebraic or Integral Equations. *Comput. Phys. Commun.* **1982**, *27*, 213−227.
(39) Berne, B. J.; Pecora, R. *Dynamic Light Scattering: With Applications to Chemistry, Biology, and Physics*; Dover Publications: New York, 2000.
(40) Eitoku, T.; Tange, M.; Kato, H.; Okazaki, T. Depolarized Dynamic Light Scattering Study of Multi-walled Carbon Nanotubes in Solution. *Mater. Express* **2013**, *3*, 37−42.
(41) Lee, H. S.; Yun, C. H. Translational and Rotational Diffusions of Multiwalled Carbon Nanotubes with Static Bending. *J. Phys. Chem. C* **2008**, *112*, 10653−10658.
(42) Zimbone, M.; Musumeci, P.; Baeri, P.; Messina, E.; Boninelli, S.; Compagnini, G.; Calcagno, L. Rotational Dynamics of Gold Nanoparticle Chains in Water Solution. *J. Nanopart. Res.* **2012**, *14*, 1308.
(43) Hoffmann, M.; Wagner, C. S.; Harnau, L.; Wittemann, A. 3D Brownian Diffusion of Submicron-Sized Particle Clusters. *ACS Nano* **2009**, *3*, 3326−3334.
(44) Pelton, M.; Liu, M.; Kim, H. Y.; Smith, G.; Guyot-Sionnest, P.; Scherer, N. F. Optical Trapping and Alignment of Single Gold Nanorods by Using Plasmon Resonances. *Opt. Lett.* **2006**, *31*, 2075−2077.
(45) Rodríguez-Fernández, J.; Pérez−Juste, J.; Liz−Marzán, L. M.; Lang, P. R. Dynamic Light Scattering of Short Au Rods with Low Aspect Ratios. *J. Phys. Chem. C* **2007**, *111*, 5020−5025.
(46) Haghighi, M.; Plum, M. A.; Gantzounis, G.; Butt, H.-J.; Steffen, W.; Fytas, G. Plasmon-Enhanced Dynamic Depolarized Light Scattering. *J. Phys. Chem. C* **2013**, *117*, 8411−8419.
(47) Glidden, M.; Muschol, M. Characterizing Gold Nanorods in Solution Using Depolarized Dynamic Light Scattering. *J. Phys. Chem. C* **2012**, *116*, 8128−8137.
(48) Broersma, S. Rotational Diffusion Constant of a Cylindrical Particle. *J. Chem. Phys.* **1960**, *32*, 1626−1631.
(49) Ortega, A.; García de la Torre, J. Hydrodynamic Properties of Rodlike and Disklike Particles in Dilute Solution. *J. Chem. Phys.* **2003**, *119*, 9914−9919.
(50) Khokhlov, A. R. *Statistical Physics of Macromolecules*; AIP Press: New York, 1994.
(51) Filippov, S. K.; Lezov, A. V.; Sergeeva, O. Y.; Olifirenko, A. S.; Lesnichin, S. B.; Domnina, N. S.; Komarova, E. A.; Almgren, M.; Karlsson, G.; Štepanek, P. Aggregation of Dextran Hydrophobically Modified by Sterically-Hindered Phenols in Aqueous Solutions: Aggregates vs. Single Molecules. *Eur. Polym. J.* **2008**, *44*, 3361−3369.
(52) Liu, T.; Troisi, A. Understanding the Microscopic Origin of the Very High Charge Mobility in PBTTT: Tolerance of Thermal Disorder. *Adv. Funct. Mater.* **2014**, *24*, 925−933.
(53) Wang, S.; Kiersnowski, A.; Pisula, W.; Müllen, K. Microstructure Evolution and Device Performance in Solution-Processed Polymeric Field-Effect Transistors: The Key Role of the First Monolayer. *J. Am. Chem. Soc.* **2012**, *134*, 4015−4018.
(54) Wu, H.; Xie, J.; Lattuada, M.; Morbidelli, M. Scattering Structure Factor of Colloidal Gels Characterized by Static Light Scattering, Small-Angle Light Scattering, and Small-Angle Neutron Scattering Measurements. *Langmuir* **2005**, *21*, 3291−3295.
(55) Zhao, H.; Chen, Q.; Hong, L.; Zhao, L.; Wang, J.; Wu, C. What Morphologies Do We Want? − TEM Images from Dilute Diblock Copolymer Solutions. *Macromol. Chem. Phys.* **2011**, *212*, 663−672.
(56) Wang, C. I.; Hua, C. C.; Chen, S. A. Dynamic Solvation Shell and Solubility of C_{60} in Organic Solvents. *J. Phys. Chem. B* **2014**, *118*, 9964−9973.
(57) Wang, C. I.; Hua, C. C. Solubility of C_{60} and PCBM in Organic Solvents. *J. Phys. Chem. B* **2015**, *119*, 14496−14504.
(58) Lee, C. K.; Hua, C. C.; Chen, S. A. An Ellipsoid-Chain Model for Conjugated Polymer Solutions. *J. Chem. Phys.* **2012**, *136*, 084901.
(59) Lee, C. K.; Hua, C. C.; Chen, S. A. Hybrid Solvents Incubated $\pi-\pi$ Stacking in Quenched Conjugated Polymer Resolved by Multiscale Computation. *Macromolecules* **2011**, *44*, 320−324.

DOI: 10.1021/acs.macromol.7b00790
Macromolecules 2017, 50, 5498−5509